nature communications

Article

https://doi.org/10.1038/s41467-026-73397-2

Absolute quantification of enantiomeric purity of sorted carbon nanotubes by correlating hyperspectral fluorescence microscopy with ensemble chiroptical spectroscopy

Received: 16 December 2025

Accepted: 8 May 2026

Published online: 26 May 2026

Check for updates

Miguel Ángel López Carrillo[1,2], Filip Desmet[1,3], Maksiem Erkens[2], Jeffrey A. Fagan[4], Ming Zheng[4], Han Li[5,6,7], Benjamin S. Flavel[5], Wim Wenseleers[2], Wouter Herrebout[1], Sofie Cambré[1] ✉ & Dmitry I. Levshov[1] ✉

Accurate determination of enantiomeric purity is essential for advancing chiral materials in nanotechnology, optoelectronics, and quantum information science. Chiroptical spectroscopic techniques provide rapid, non-destructive measurements of enantiomeric excess (ee), but their use for complex systems like single-walled carbon nanotubes (SWCNTs) is limited by the lack of enantiopure references for calibration. Here we demonstrate an absolute approach combining hyperspectral imaging (HSI) with single-nanotube counting statistics and ensemble chiroptical spectroscopy such as electronic circular dichroism (ECD) and Raman optical activity (ROA) to quantify ee without requiring such standards. Analysis of thousands of individual nanotubes reveals sensitivity of HSI and chiroptical responses to synthesis, purification, and SWCNT concentration, highlighting pronounced source-dependent inhomogeneity. Nevertheless, universal calibration curves for ECD and ROA intensities are established from the purest, most uniform enantiomer-sorted samples. This methodology is extendable to other SWCNT chiralities and chiroptical techniques, enabling quantitative enantiomer sorting and systematic investigations of chirality-dependent properties and applications.

Chirality, the property of matter and waves to exist in two spatially non-superimposable left- and right-handed forms, has emerged as an important concept in modern nanoscience[1]. Chiral nanomaterials exhibit quantum phenomena that are sensitive to handedness, ranging from chirality-induced spin selectivity[2,3], to selective interactions with chiral entities[4–6], such as molecules, photons, electrons, and phonons. These effects enable applications from the detection[7] and separation[8] of chiral molecules in biology and chemistry to the manipulation of circularly polarized light[9], a key functionality for quantum computing[2], spintronics[10,11], and optoelectronics[12].

Among the most promising chiral nanomaterials are single-wall carbon nanotubes[13] (SWCNTs), chemically stable one-dimensional structures with exceptional electronic and optical properties[14]. While some SWCNTs adopt achiral zigzag or armchair geometries, most

A full list of affiliations appears at the end of the paper. ✉e-mail: sofie.cambre@uantwerpen.be; dmitry.levshov@uantwerpen.be

occur in mirror-image chiral forms, or enantiomers (Fig. 1a; also showing existing enantiomer naming conventions). Recent advances in sorting[15–18] have enabled large-scale separation of SWCNTs into their enantiomeric forms. However, to fully exploit these samples in chirality-specific applications, it is essential to determine their enantiomeric purity, typically expressed as enantiomeric excess $ee(\%) = [(C_+ - C_-)/(C_+ + C_-)] \times 100$, where C_+ and C_- are the amounts of (+)- and (-)- enantiomers[19].

Several techniques can distinguish SWCNT enantiomers, including scanning tunneling microscopy[20], transmission electron microscopy[21–23], atomic force microscopy of aligned SWCNTs[24,25], and chiroptical spectroscopies such as electronic circular dichroism (ECD)[26–28], Raman optical activity (ROA)[29–31], and Rayleigh scattering circular dichroism[32]. While high-resolution microscopy techniques provide direct structural information, they are inherently low-throughput and require extensive data collection for ee measurements on bulk SWCNTs. Consequently, chiroptical spectroscopy has become the method of choice[33,34]. Its broader application, however, has been limited by the absence of 100 % enantiomerically pure SWCNT standards. Early studies defined purities relative to the best available samples, leading ee benchmarks to shift as sorting techniques improved. This limitation was addressed by Wei et al.[33], who exploited subtle shifts[33–35] in optical transition energies caused by preferential interactions of SWCNT enantiomers with specifically-designed enantiomerically pure chiral surfactants. They demonstrated that ECD intensity can be calibrated against ee values derived from these shifts, establishing ECD as a rapid and direct method for ee estimation, a strategy now increasingly adopted by the SWCNT community.

Despite these advances, the use of chiroptical spectroscopy for SWCNT ee characterization remains limited. Several chiroptical techniques commonly applied to molecular systems[9,19,36,37] including ROA, vibrational circular dichroism (VCD), and circularly polarized luminescence (CPL), have not been systematically explored for SWCNTs. Even for widely used ECD, reliability can be uncertain due to the complex nature of SWCNT spectra, which contain multiple overlapping bands and scattering- or impurity-related backgrounds. Cross-validation with independent methods is therefore essential. Additional challenges arise from extrinsic factors, such as post-synthesis processing or molecular filling, whose effects on chiroptical signals are still poorly understood.

Here, we introduce a strategy that combines complementary chiroptical techniques, ECD and ROA, with hyperspectral imaging[35] (HSI) to achieve absolute ee quantification of enantiomer distribution by measuring the emission energies and linewidths for thousands of individual nanotubes. This single-nanotube-level analysis enables determination of the absolute ee of SWCNT samples and its correlation with ECD and ROA intensities establishes an absolute calibration for both techniques (Fig. 1b). We applied this approach to seventeen enantiomer-sorted (6,5) SWCNT samples (Fig. 1c, d) derived from different synthesis methods (high-pressure CO disproportionation (HiPCO)[38] and cobalt-molybdenum catalyst (CoMoCAT[39])) and with varying enantiomeric purity, processing history and filling state (empty[18,40–42], water-filled[18,40–42], or alkane-filled[43–46]) (see Supplementary Table 1 for sample details). HSI, ECD, and ROA revealed significant differences in sample responses, yet a universal intensity calibration curve was established for all sample types using the purest HiPCO SWCNTs. We also identified SWCNT concentration as a critical factor for ee estimation by chiroptical spectroscopy, particularly in ROA, where high concentrations introduce spectral artifacts due to reabsorption and ECD-Raman effects[47,48].

Results and discussion

Enantiomeric purity determination via HSI

The strategy for determining ee in enantiomer-sorted SWCNT samples by HSI relies on direct imaging and counting of individual enantiomers. SWCNTs are first dispersed with a chiral surfactant (sodium deoxycholate, DOC), highly diluted, and then immobilized in a gel matrix (Fig. 2a), which does not affect their optical properties[35]. The gel-embedded SWCNTs are then imaged by hyperspectral fluorescence microscopy, registering the near-infrared (NIR) emission from ~10^4 individual (6,5) SWCNTs. The resulting hyperspectral images are processed using automated nanotube recognition via a convolutional neural network, followed by spectral fitting (Supplementary Note 3.1 and ref. 35.), to extract the emission energy, full width at half maximum (FWHM) of the emission peak, and length of each individual nanotube. These parameters are compiled into 2D bivariate histograms (Fig. 2a), where the color scale represents the number of tubes linearly weighted by nanotube length (i.e., a measure for number of carbon atoms; with a spatial resolution of 624 nm[35]). This weighting is essential for accurate comparison with chiroptical spectroscopy signals.

The HSI histograms depend strongly on the type of SWCNT samples, such as the synthesis method or filling state. For example, representative histograms for (+) and (−) enantiomers from (a mixture of empty and water-filled) HiPCO, (water-filled) CoMoCAT, and alkane-filled CoMoCAT samples are shown in Fig. 2b–g (see Supplementary Fig. 4 for other cases). HiPCO samples display four distinct populations in the high-energy zone (> 1.252 eV, labeled H in Fig. 2a), originating from (+)/(-) empty (E) and (+)/(-) water-filled (W) enantiomers (W + , W−, E + , E−), as found previously for chirality-sorted (but not enantiomer sorted) and density-gradient ultracentrifuged (DGU) samples[35]. In addition to these established features, we detect two new weaker components in the low-energy zone (< 1.252 eV, labeled L in Fig. 2a). These features are more pronounced in CoMoCAT samples where SWCNTs exhibit larger variability in FWHM and emission energies, leading to broad overlapping "tails" between zones L and H. Additional DGU experiments reveal that the nanotubes displayed in zone L have higher density (Supplementary Note 4.2) leading us to tentatively assign zone H to pure individualized SWCNTs, and zone L to more "defective" nanotubes, possibly functionalized or coated with impurities such as amorphous carbon. These defective SWCNTs were not observed in ref. 35., primarily due to the choice of starting SWCNT batch combined with an additional DGU purification step.

By comparison, alkane-filled CoMoCAT nanotubes display two sharp (+) and (−) peaks with narrow FWHM and lower emission energies. Since alkane filling involves an air-oxidation step that removes impurities, we assign these peaks to pure individualized nanotubes whose photoluminescence (PL) spectra are red-shifted due to strain induced by alkane filling[43,44] (see Supplementary Note 5).

Further analysis of the HSI histograms shows that, with the chiral DOC surfactant used in this work, (+) and (−) enantiomers can be reliably distinguished and quantified only in HiPCO samples. This is most clearly illustrated by the ≈3.5 nm (≈ 5 meV) shift between the two enantiomers in the absorption and PL spectra (Fig. 2h, i). In contrast, CoMoCAT samples do not allow for a clear identification of the four contributions (W + , W−, E + , E−) in zone H, due to greater variability in FWHM and emission energies, which results in broad overlapping distributions (Fig. 2d, e). Alkane-filled ($C_{24}H_{50}$@) CoMoCAT samples present similar challenges for ee quantification, as water-filled species also contribute to the histograms in zone H (visible as weak broadened peaks; see also peaks in the high-resolution radial breathing mode (RBM) spectra, Supplementary Fig. 21b). However, these peaks cannot be reliably fitted with the available statistics.

Future HSI studies may overcome these limitations by employing alternative chiral surfactants, such as flavin mononucleotide[33], to enhance spectral separation enabling more accurate extraction of both enantiomer contributions. Nevertheless, HiPCO samples with DOC surfactant provide a basis for ee quantification, and as shown below, the so-established calibration can be extended to all other sample types.

https://doi.org/10.1038/s41467-026-73397-2

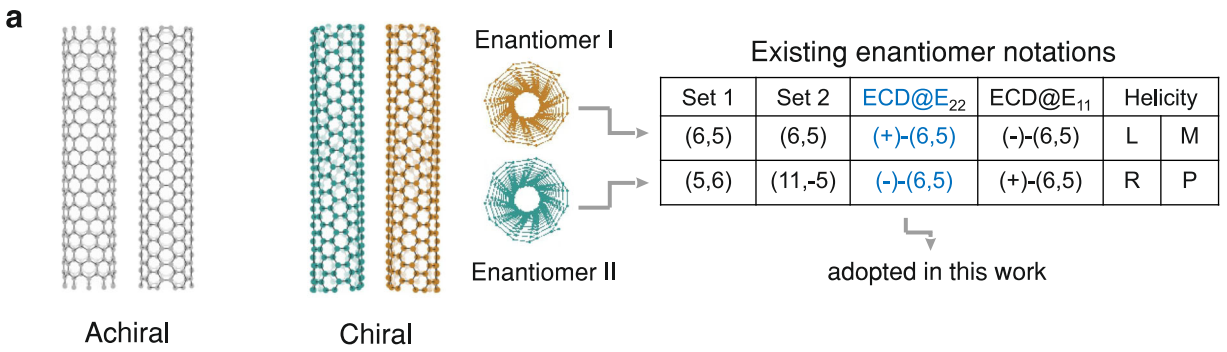

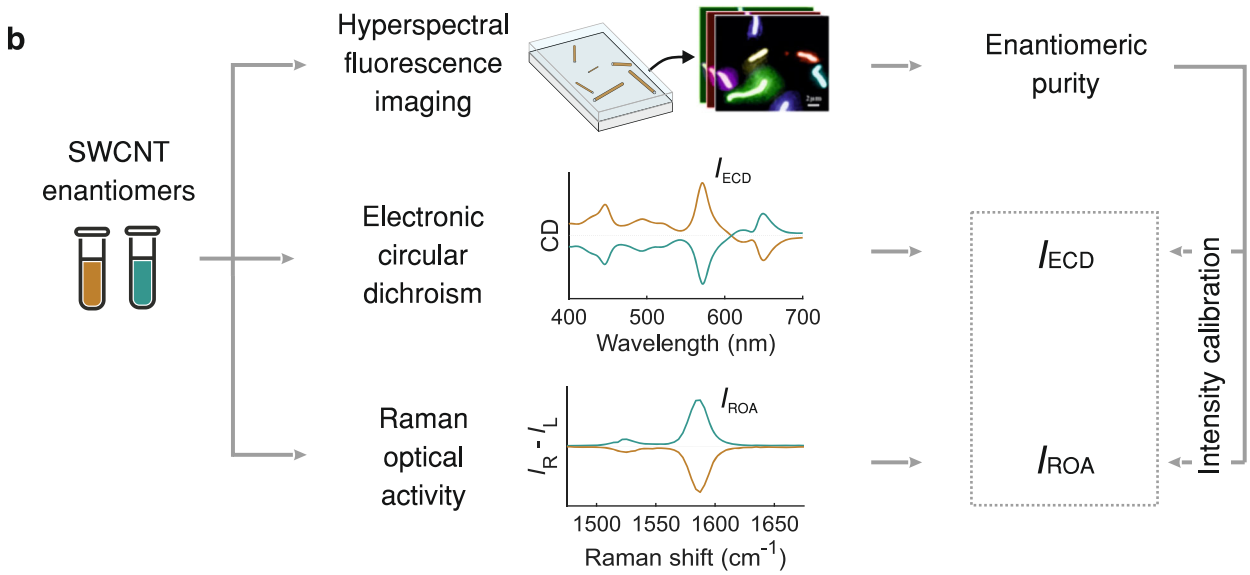

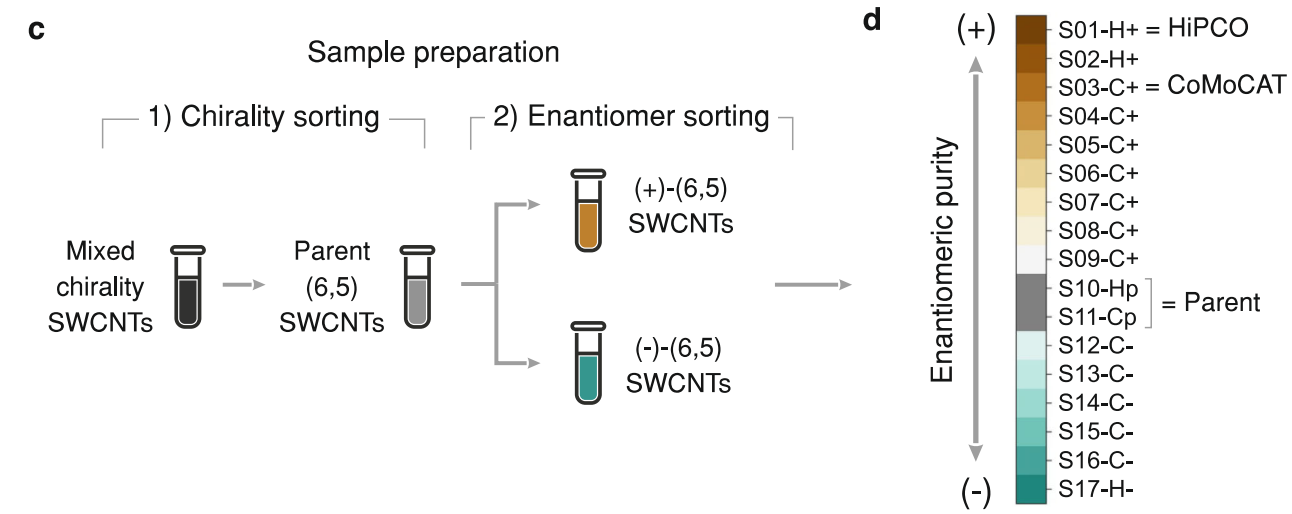

Fig. 1 | Schematic overview of the samples. a Schematic representation of achiral zigzag and armchair SWCNTs (left) alongside the two chiral (6,5) SWCNT enantiomers, with commonly used naming conventions from the literature; the notation adopted in this study is highlighted in blue (see Supplementary Note 2.2). **b** Overview of the experimental workflow for calibrating and quantifying the enantiomeric purity of sorted SWCNTs using HSI, ECD, and ROA. The color in the spectra represents the type of enantiomer. **c** Illustration of the enantiomer sorting process applied to mixed-chirality SWCNT samples to isolate (+)- and (−)-(6,5) SWCNTs. **d** List of the enantiomer-sorted samples analyzed in this work, along with the labels and color scales used to represent them. More details can be found in Supplementary Table 1.

https://doi.org/10.1038/s41467-026-73397-2

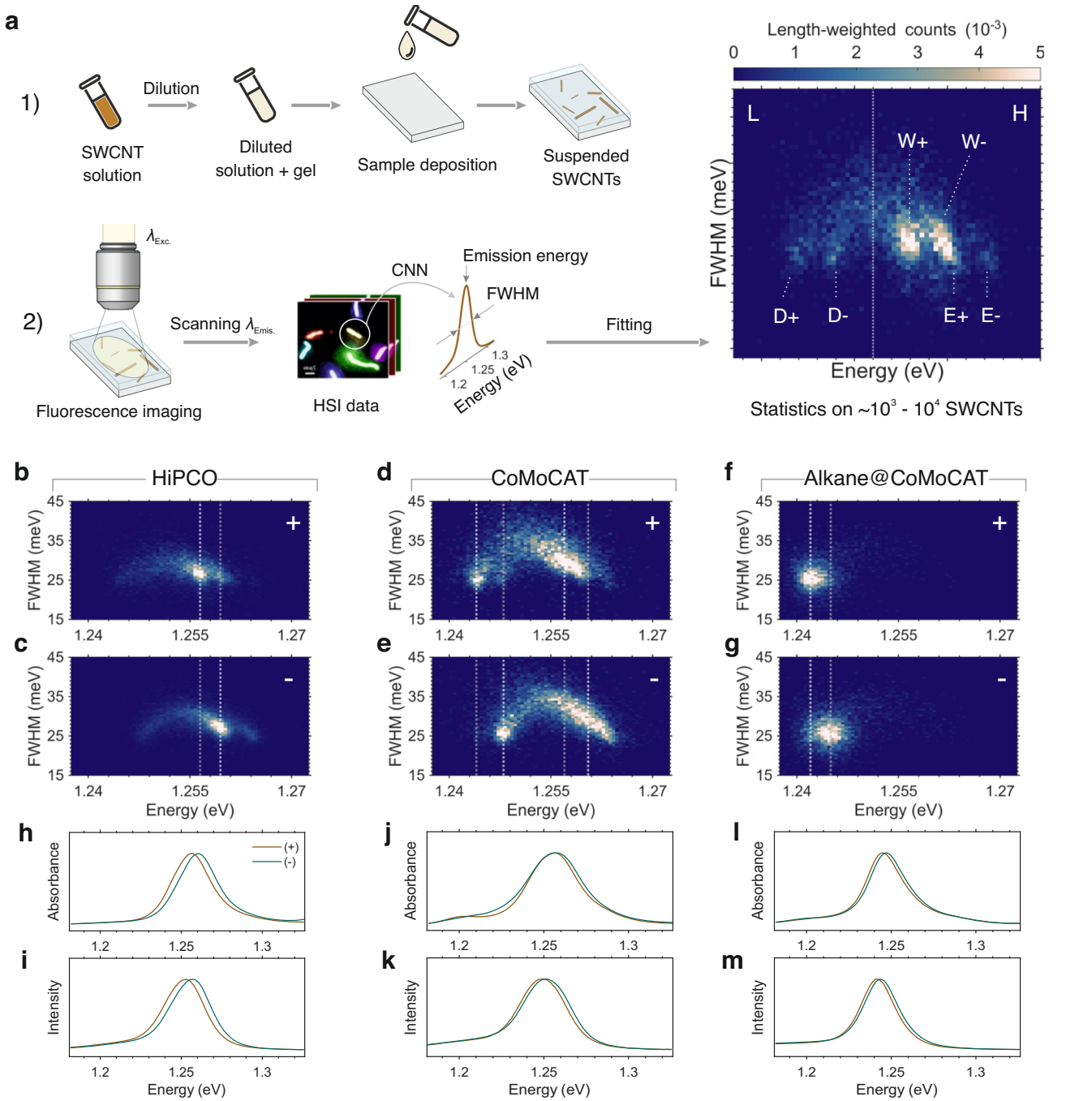

Fig. 2 | Overview of HSI characterization. a Schematic of the HSI characterization workflow, comprising preparation of gel-embedded SWCNTs, acquisition of HSI data, automated nanotube identification using a convolutional neural network (CNN), spectral fitting to extract emission energy and peak FWHM, and compilation of these parameters for ~10^3–10^4 individual nanotubes into 2D bivariate histograms. The histograms reveal two distinct emission-energy regions at 1.24–1.25 eV and 1.25–1.27 eV, referred to as zone L and zone H. **b**–**g** Bivariate histograms for representative (+)- and (−)-(6,5) SWCNTs from HiPCO (S01-H+ and S17-H-, **b, c**), CoMoCAT (S04-C+ and S15-C-, **d, e**), and alkane-filled CoMoCAT (S03-C+ and S12-C-, **f, g**) samples. Vertical lines mark the positions of the (+) and (−) clusters. Histograms for other samples are shown in Supplementary Fig. 4. For each histogram, *n* equals the number of individually identified SWCNTs contributing to the statistics: S01-H+ ($n = 9033$), S17-H− ($n = 14311$), S04-C+ ($n = 9218$), S15-C− ($n = 12047$), S03-C+ ($n = 4022$), and S12-C− ($n = 4820$). **h, j, l** Absorption and **i, k, m** photoluminescence (PL) spectra zoomed in on the S_{11} region (see full spectra in Supplementary Figs. 2,3), for representative (+)- and (−)-(6,5) SWCNTs across HiPCO (**h, i**), CoMoCAT (**j, k**), and alkane-filled CoMoCAT samples (**l, m**), with notable spectral shifts between enantiomers primarily observed in HiPCO SWCNTs. The brown and dark cyan colors represent (+) and (-) enantiomers, respectively. Source data are provided as a Source Data file.

To estimate ee, we fitted the experimental HiPCO histograms using six 2D skewed normal distribution functions (Supplementary Note 4.3). Representative examples of experimental histograms and their corresponding fits are shown in Fig. 3a–f for the S01-H + , S10-Hp, and S17-H− samples, with empty (E), water-filled (W) and defective (D) (+) and (-) contributions clearly indicated. As the histograms represent individual nanotube counts weighted by their length, the fitted amplitudes (areas) of these functions are proportional to the number of carbon atoms for each enantiomer species in the sample, allowing us to calculate the relative content of each enantiomer (Fig. 3g, in percent). The resulting ratios of empty, water-filled, and defective species agree well with high-resolution Raman analysis of the

https://doi.org/10.1038/s41467-026-73397-2

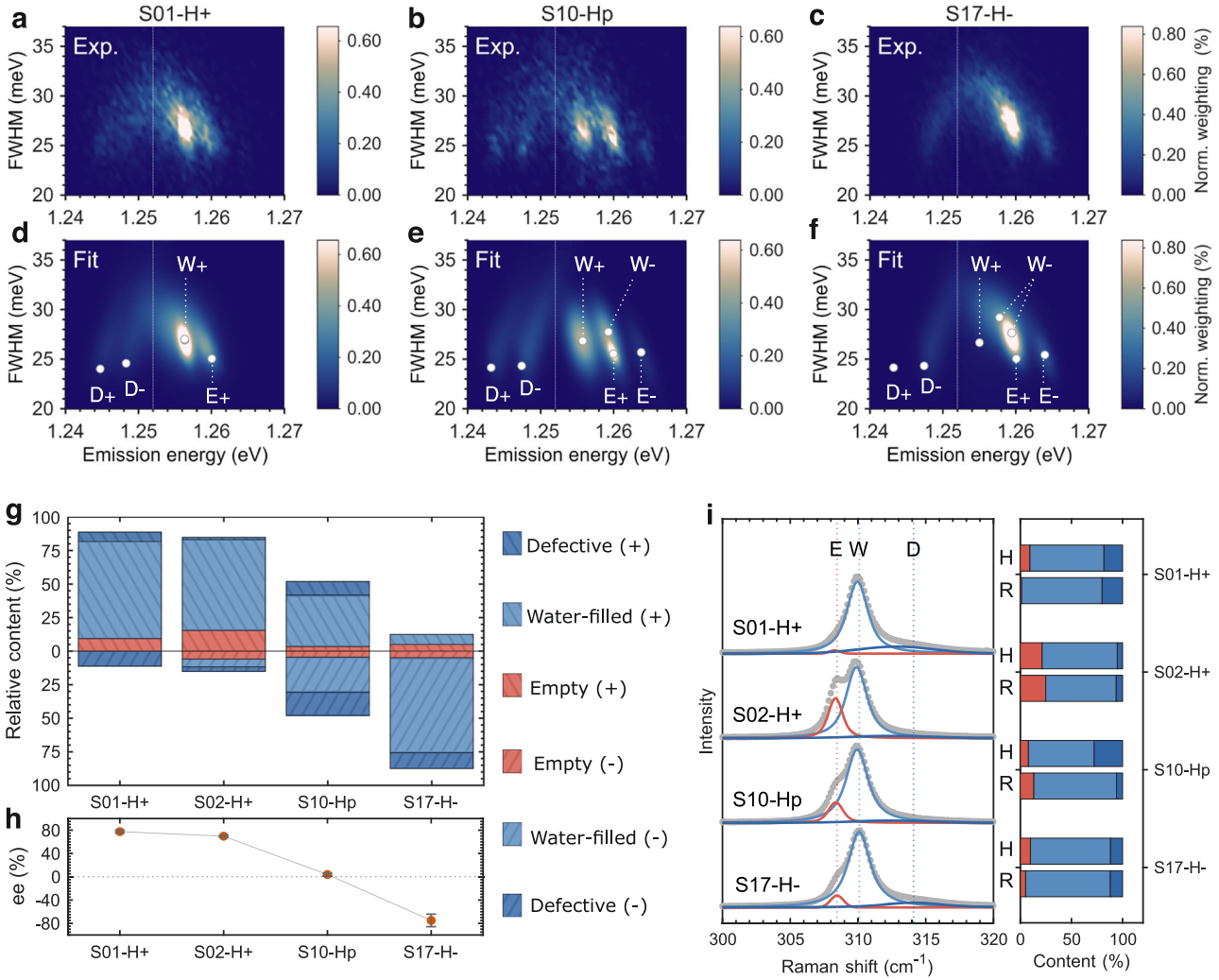

Fig. 3 | Determination of enantiomeric purity using HSI. a–c Experimental 2D HSI histograms of the HiPCO samples S01-H + , S10-Hp and S17-H-, weighted by SWCNT length to serve as a measure of the total mass fractions (number of carbon atoms) of the different species; The histograms include data from n = 9033, 6338, and 14311 nanotubes respectively. **d–f** Corresponding fitted 2D histograms for S01-H + , S10-Hp and S17-H- samples with six species identified: water-filled (W + , W-), empty (E + , E-), defective (D + , D-) (+)- and (-)-(6,5) SWCNTs. For S17-H−, two 2D Gaussian functions were required to fit the W− species, indicated by white dots (see Supplementary Figs. 7-8 for the goodness of the fit); **g** Relative content of D+ and D- (dark blue), W+ and W- (blue), and E+ and E- (red) species in the analyzed samples extracted from the fitted HSI intensity values; **h** Enantiomeric excess (ee) for the four studied HiPCO samples, calculated by summing the contributions in **g**. Error bars represent ±1σ uncertainties derived from the errors of the fitted 2D Gaussian intensities, with error propagation; **i** RBM region (left) of high-resolution Raman spectra for S01-H + , S02-H + , S10-Hp, and S17-H−, showing peak positions of empty (E), water-filled (W), and defective (D) fractions. Right: comparison of the content of E (red), W (blue), and D (dark blue) fractions determined from HSI (H) and RBMs (R). Source data are provided as a Source Data file.

RBMs (Fig. 3i, Supplementary Note 7.1), where these contributions are represented in red, blue, and dark blue, respectively. For example, S02-H+ shows the highest fraction of empty nanotubes, while S01-H+ and S17-H− are dominated by water-filled SWCNTs. By summing the empty, water-filled, and defective contributions for each enantiomer, we derived the ee values, reported in Fig. 3h and summarized in Supplementary Table 4.

Calibration of chiroptical response with HSI-derived ee

We directly correlated the HSI-derived ee values with the chiroptical ECD and ROA responses of the same HiPCO samples (Fig. 4). Representative absorption and normalized ECD spectra are shown in Fig. 4b, c, and Raman and ROA spectra in Fig. 4d, e for S01-H + , S02-H + , S10-Hp, and S17-H−. The absorption and ECD spectra display characteristic interband transitions of (6,5) SWCNTs (S_{11}, S_{22}, S_{33}, S_{44}) as well as cross-band transitions (S_{21}, S_{31}, most prominent in the ECD spectra) in agreement with previous assignments[26]. In the Raman and ROA spectra, prominent features include the G-band (≈ 1590 cm^{-1}), the 2D-band (≈ 2600 cm^{-1}), the intermediate frequency mode (IFM, ≈1050 cm^{-1})[49], and the TO + ZO combination mode (≈ 1900 cm^{-1})[50]. The RBM is off-resonance at this excitation and thus weak. The sign of all ROA modes is opposite to that of ECD at the excitation wavelength, consistent with resonance ROA theory in the single-state limit[51].

To account for SWCNT concentration differences[18], the raw ECD and ROA responses are typically normalized by the height of the S_{22} and G+ peaks, respectively. Figure 4f illustrates this normalization for ECD at the S_{22} transition. We found that two normalization approaches exist: using the peak height alone or including the underlying absorption background (solid vs. dashed vertical lines in Fig. 4f, bottom). These approaches lead to two distinct calibration curves when relating the chiroptical responses to the absolute ee values from the HSI measurements, as shown by the solid and dashed lines representing calibration without or with the background, respectively.

https://doi.org/10.1038/s41467-026-73397-2

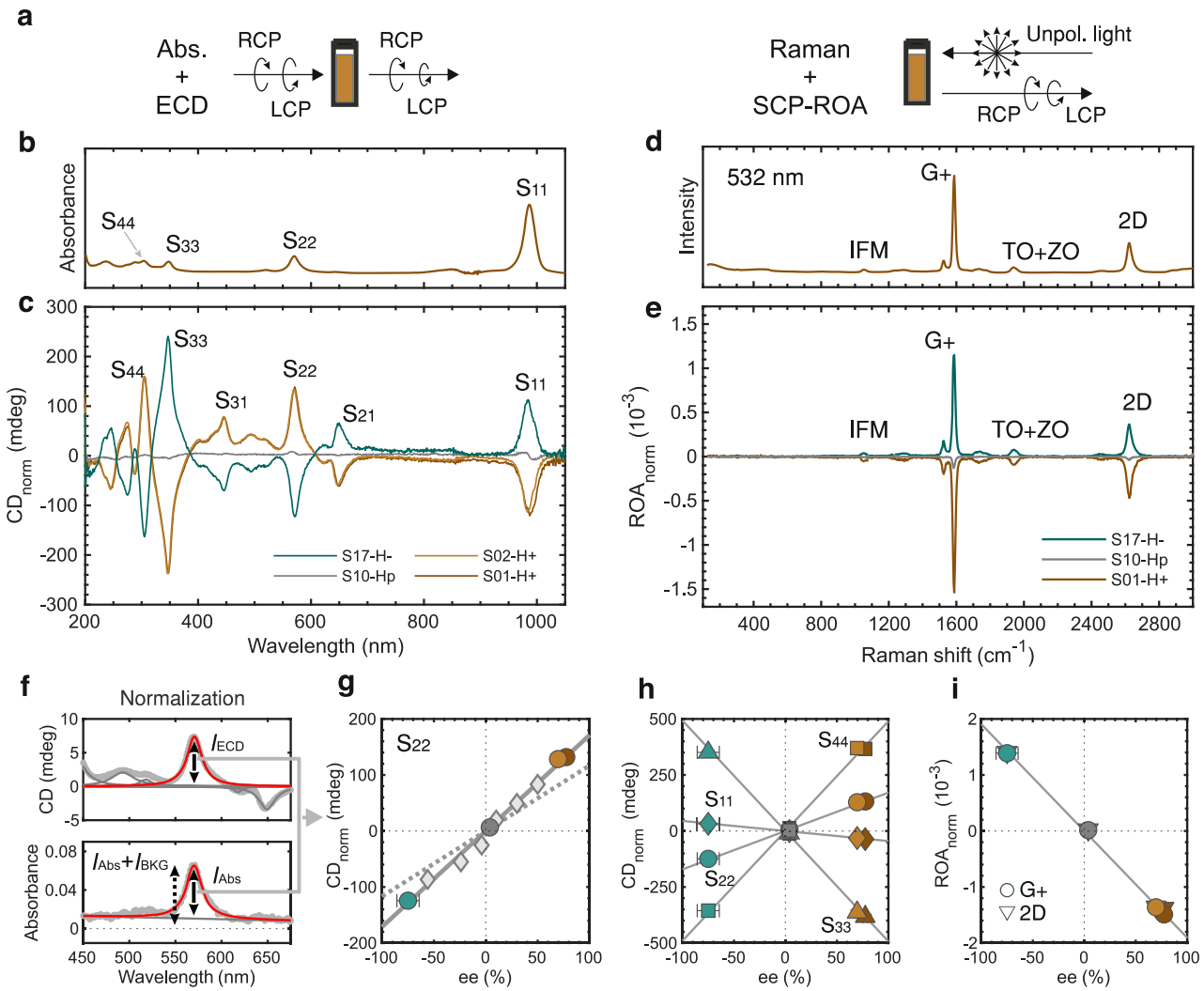

Fig. 4 | Calibration of ECD and ROA intensities. a Schematic of the ECD and scattered circular polarization ROA processes. **b** Absorbance and **c** ECD spectra of enantiomer-sorted (6,5) HiPCO SWCNT samples, with the main electronic transitions (S_{11}, S_{22}, S_{33}, S_{44}) and cross-band transitions (S_{21}, S_{31}) indicated. Colors denote sample type: S01-H+ (brown), S02-H+ (light brown), S10-Hp (gray), and S17-H− (dark cyan), and are used consistently in all subsequent panels **d** Resonant Raman and **e** ROA spectra (532 nm excitation, 2.33 eV) of S01-H + , S10-Hp and S17-H− samples. Prominent Raman bands are highlighted. (**f**) Illustration of the normalization procedure, showing peak heights with and without the baseline. **g** Correlation between normalized ECD intensity of the S_{22} peak and ee determined from HSI. Data from Wei et al[33]. (gray diamonds), reanalyzed using the alternative normalization method, are included for comparison; Dashed and solid lines represent the calibration of ECD normalized with or without the background, respectively. **h** ECD calibration curves (without background) for the four main transitions of (6,5) SWCNTs: S_{11} (diamond), S_{22} (circle), S_{33} (triangle) and S_{44} (square). CD_{norm} values for S01-H + , S02-H + , S10-Hp, and S17-H− were obtained by first fitting individual spectra to extract CD_{norm}, followed by averaging over $n = 2, 2, 2$, and 4 independently recorded spectra, respectively. Error bars (smaller than symbol size) represent $\pm 1\sigma$ uncertainties from fitted errors of individual CD_{norm} values, with propagation during averaging. (**i**) Correlation between the normalized ROA intensities of the G+ and 2D modes and the enantiomeric excess determined from HSI. Parameters of the linear fits are provided in Supplementary Table 7. ROA_{norm} values were obtained from fits to a single spectrum for each sample ($n = 1$, acquisition time ≈60 min). Error bars (smaller than symbol size) represent $\pm 1\sigma$ standard deviations from spectral fitting. Source data are provided as a Source Data file.

From the first calibration (solid line, Fig. 4g), we estimate that a fully enantiopure (+)-(6,5) sample (100% ee) corresponds to $CD_{norm} = (174 \pm 5)$ mdeg, whereas the latter (gray dashed line) reproduces the earlier calibration established by Wei et al.[32] predicting the highest purity at (119 ± 9) mdeg[33]. Interestingly, when re-examining the CD and absorption spectra of Wei et al.[33] using peak height only normalization (Supplementary Note 6.3), we obtain CD_{norm} values that align with the first calibration curve (gray diamonds, Fig. 4g). This highlights the importance of applying a consistent normalization method when comparing results across studies[18,26,33,52]. Note that normalizing by the peak height without background may be advantageous, as it minimizes deviations from the unaccounted baseline in the absorption spectra (be it instrumental or sample-related, including a typical scattering origin).

In addition, we applied the calibration to all resolved transitions (S_{11}, S_{22}, S_{33}, S_{44}) of enantiomer-sorted (6,5) SWCNTs, as shown in Fig. 4h, with each transition normalized to its own absorption peak, yielding four distinct calibration curves (see Table 1 for fit parameters).

We further established calibration curves for the main Raman-active modes of (6,5) SWCNTs: G + , G−, 2D, IFM, and TO + ZO. Since they span a wide range of frequencies (1000 to 2600 cm^{-1}), we can assess resonance effects on the enantiomeric purity determined from ROA. Remarkably, the ROA_{norm} values for all modes show minimal dependence on resonance and converge to nearly identical values for each sample (Supplementary Fig. 26). Figure 4i illustrates this using the G+ and 2D modes, whose values are practically indistinguishable (note that the data were corrected by subtracting a small constant offset, attributed to residual contributions from impurities; see

Supplementary Fig. 27). From this calibration, we estimate that a fully enantiopure (+)-(6,5) sample (100% ee) corresponds to a ROA_{norm} of $-(1.90 \pm 0.05) \times 10^{-3}$ (for 532 nm illumination).

Table 1 | Fitted parameters of the calibration curves for ECD and ROA, defined as ee = $a_H \times CD_{norm}$ or ee = $a_H \times ROA_{norm}$

Technique	Type	a_H
ECD	S_{11}	−2.174 ± 0.047
	S_{22}	0.575 ± 0.017
	S_{33}	−0.202 ± 0.005
	S_{44}	0.203 ± 0.009
ROA	G+	$(-5.26 \pm 0.14) \times 10^{-5}$
	2D	$(-5.49 \pm 0.06) \times 10^{-5}$

The coefficients a_H were obtained from fits using normalized peak heights (excluding the background by fitting). Fits using normalized peak areas (a_A) are reported in Supplementary Note 8. For ECD, a_H has units of $mdeg^{-1}$, whereas for ROA it is dimensionless. The uncertainties correspond to one standard deviation.

Finally, we note that all established calibration curves exhibit clear linear relationships between chiroptical signals and ee, when using proper measurement conditions (i.e., sample concentration, see further). This contrasts with recent studies on interacting systems[53–55] which reported non-linear ee dependences due to strong enantiomer–enantiomer interactions. Our measurements involve either liquid dispersions with minimal enantiomer interactions (for ECD and ROA) or highly diluted, gel-suspended samples with well-separated nanotubes (for HSI), making non-linear effects negligible for these SWCNT samples.

Establishing the universality of chiroptical calibration

We next investigated the dependence of the chiroptical properties of enantiomer-sorted SWCNTs on the synthesis method and filling state. This is best illustrated by focusing on the S_{22} region of the ECD spectra (Fig. 5a) and the G-band region of the ROA spectra (Fig. 5b). To quantify the variations in optical properties among these samples, the spectra were fitted following the procedure described in Supplementary Notes 6.2 and 7.2, and the resulting FWHM values are plotted in Fig. 5c, d (as a function of wavelength for absorption and ECD) and in Fig. 5e, f

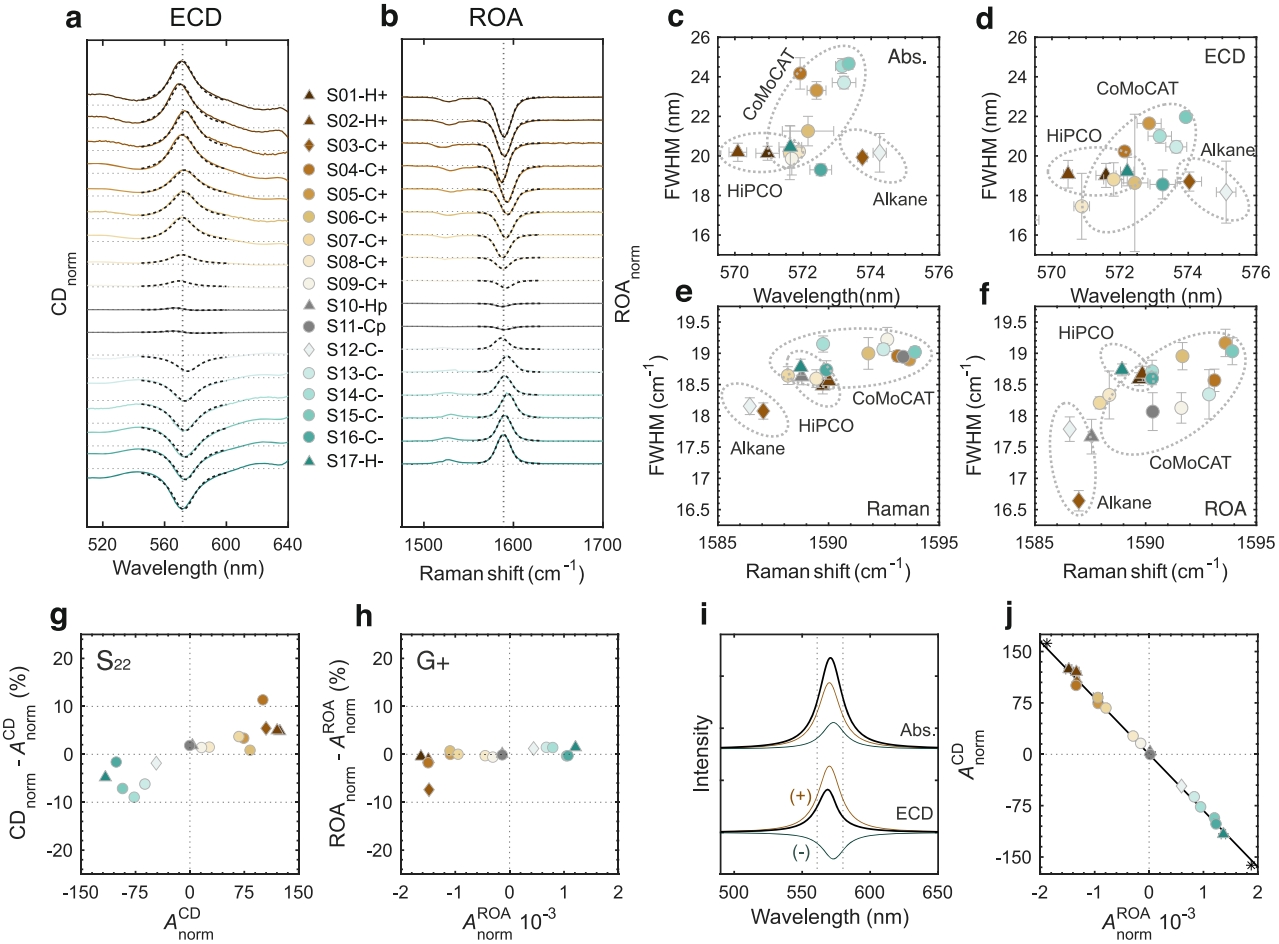

Fig. 5 | Statistical analysis of ECD and ROA spectra. a Normalized ECD spectra at the S_{22} transition and **b** ROA spectra in the G-band region for all studied (6,5) enantiomer-sorted SWCNTs. Colors denote individual samples (see labels between **a** and **b**) and are used consistently throughout the figure. Correlation of FWHM with peak center for **c** absorption and **d** ECD spectra, and for **e** Raman and **f** ROA spectra in the G+ region; HiPCO, CoMoCAT and alkane@CoMoCAT are represented by triangles, circles and diamonds, respectively. Ellipses are guides to the eye highlighting SWCNT types. Parameter values for (**c**) were obtained as mean values of spectral fits for each sample (see exact n in Supplementary Note 6.2), with error bars representing ±1σ standard deviations of the fitted values. For (**d**), the same procedure was applied after exclusion of outliers identified using Tukey's quartile criterion. Raman and ROA parameters were extracted from single spectra for each sample (acquisition time ≈60 min). Error bars in (**e, f**) represent ±1σ uncertainties from spectral fitting. **g** Dependence of normalized S_{22} peak height on normalized S_{22} peak area, derived from the fits in (**a**). **h** Dependence of normalized G+ peak height on normalized G+ peak area, derived from the fits in (**b**). **i** Simulated ECD and absorption spectra illustrating how summation or subtraction of enantiomer contributions affects linewidth; **j** Correlation between normalized ECD and ROA intensities for all studied (6,5) enantiomers. Source data are provided as a Source Data file.

https://doi.org/10.1038/s41467-026-73397-2

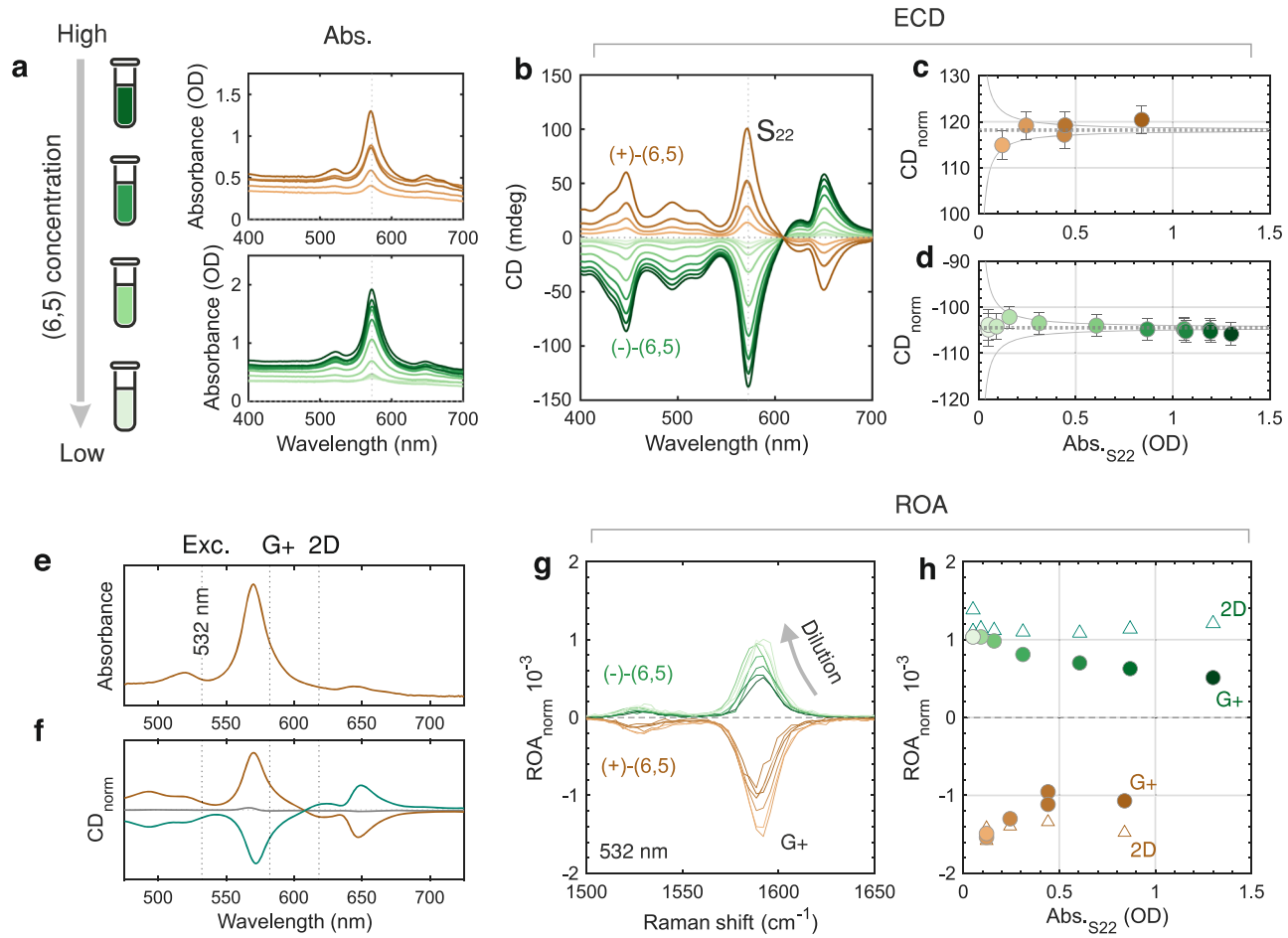

Fig. 6 | Concentration dependence of ECD and ROA intensities. a Absorbance and **b** ECD spectra for (+)-(6,5) (brown) and (−)-(6,5) (green) CoMoCAT samples. **c**, **d** Normalized S_{22} ECD intensity as a function of the S_{22} absorption peak height for the (+)-(6,5) (**c**) and (−)-(6,5) (**d**) enantiomers. Error bars in (**c**, **d**) represent ±1σ fit uncertainties of the S_{22} ECD intensity extracted from individual spectra. Each point corresponds to a single spectrum recorded from the same sample at a different concentration; no averaging over repeated measurements was performed. **e** Absorption and **f** ECD spectra of the studied (6,5) enantiomers, with indicated energies for laser excitation (2.33 eV) and the G- and 2D-band scattered photons. **g** ROA spectra of (−)-(6,5) (green) and (+)-(6,5) (brown) samples, showing changes with SWCNT concentration. **h** Dependence of fitted ROA intensities for the G+ (circles) and 2D-band (triangles) of (−)-(6,5) (green) and (+)-(6,5) (brown) samples on SWCNT concentration, represented by the S_{22} peak height in the corresponding absorption spectra. Source data are provided as a Source Data file.

(as a function of Raman shift for Raman and ROA). For clarity, HiPCO, CoMoCAT, and alkane-filled CoMoCAT samples are grouped with ellipses.

The three sample types are readily distinguishable in these plots due to the shifts in wavelength or frequency and differences in line broadening. These variations arise from compositional differences (different ee or filling), as also revealed by HSI. Interestingly, in some samples, particularly CoMoCAT, the linewidths of the S_{22} and G+ peaks are slightly larger in absorption and Raman than in their chiroptical counterparts (ECD and ROA). This can be tentatively explained by how the (+) and (−) contributions combine: in absorption and Raman, their intensities add, broadening the peaks, whereas in ECD and ROA, their signals subtract, narrowing the total spectrum (see simulated spectra in Fig. 5i). The difference should be more pronounced in samples with lower ee, where the amplitudes of (+) and (−) contributions become comparable.

These linewidth differences can affect ee estimations, depending on whether chiroptical signals are normalized by peak height or peak area. Figure 5g, h show the deviations of CD_{norm} relative to A^{CD}_{norm} (i.e., the S_{22} peak area in CD normalized by the absorption peak area) and of ROA_{norm} relative to A^{ROA}_{norm} (i.e., the G+ peak area in ROA normalized by the Raman peak area), plotted on the y-axis in percent. Clear deviations are observed, with the largest in ECD, up to ≈10%. For ROA, the G+ mode shows the smallest deviation, although other modes can exhibit substantially larger discrepancies. Our simple simulations further suggest that peak-area normalization yields values closer to the true ee, indicating that it may provide a more reliable basis for ee estimation in highly inhomogeneous samples (see Supplementary Table 7 for corresponding fit parameters).

Finally, we found that the normalized ECD and ROA data for the S_{22} transition and G+ mode across all 17 studied samples are well correlated and fall on a single linear trend, independent of synthesis method or filling state (Fig. 5j). This demonstrates that neither the presence of defective SWCNTs in CoMoCAT (zone L, Fig. 2b) nor alkane filling significantly affects chiroptical intensities. Therefore, the intensity calibration curves established for HiPCO samples (Figure 4g–i) are broadly applicable, confirming the robustness and universality of our HSI-based ee calibration.

Dependence of chiroptical intensities on SWCNT concentration

Finally, we present how SWCNT concentration influences the accuracy of ee determination from chiroptical measurements. As an example, Fig. 6a, b shows absorption and ECD spectra of S04-C+ and S15-C− recorded at different concentrations. After normalizing the ECD signal to the S_{22} peak height (excluding background), we observed no systematic dependence of CD_{norm} on concentration (Fig. 6c, d).

Significant deviations occurred only at low concentrations, where instrumental effects such as baseline drift (≈0.5 mdeg) became comparable to the weak CD signals, leading to large fluctuations in the normalized values (see diverging gray lines in Fig. 6c, d).

However, the concentration effect appears much more pronounced for ROA measurements: at 532 nm decreasing SWCNT concentration led to a doubling of the ROA signal for both (+)-(6,5) and (−)-(6,5) enantiomers (Fig. 6g, h). The observed enhancement is attributed to intrinsic chiroptical effects, specifically, photon reabsorption and the ECD-Raman effect, both known from studies of other chiral molecules[47,48]. They occur when either the incident or scattered photons are absorbed by the medium with a strong ECD response resulting in a modification of the ROA signals. However, such modification depends on the scattered photon energy of the vibrational mode relative to the ECD peak maximum (Fig. 6e, f): both laser excitation (vertical line labeled "Exc.") and 2D-band photons lie in a region of low CD response, implying minimal absorption of polarized light, while the G-band scattered photon energy lies near the S_{22} maximum and is thus highly prone to reabsorption (Supplementary Notes 7.3 and 7.4).

In principle, this ECD–Raman contribution can be corrected numerically if the sample concentration is known precisely[47,48,56]. However, for SWCNTs the absorption cross-sections are currently known only within an order of magnitude[57–60], making such a correction unreliable. Therefore, to minimize these artifacts in ROA, we recommend (i) working at low SWCNT concentrations as reflected in the optical density (OD < 0.67 cm^{-1}) and (ii) placing the laser focus close to the ROA cell window, as the measured intensity varies with focus depth (Supplementary Note 7.4). By contrast, for ECD, reliable ee determination is best achieved at medium concentrations, which provide good signal-to-noise while keeping instrumental effects such as baseline drift negligible.

Practical workflow for ee determination

Once the ECD or ROA responses are calibrated against the ee using HSI for a given *(n,m)* SWCNT species (as shown above for the most commonly used (6,5) SWCNTs), the determination of ee in unknown sorted samples of the same chirality becomes straightforward and requires only a single spectroscopic measurement.

In practice, the workflow consists of the following steps. First, the ECD or ROA spectrum of the sample is recorded under the same experimental conditions used for the calibration dataset (e.g., low sample concentrations for ROA measurements to avoid ECD–Raman effects, see previous section). Second, the relevant spectral parameter is extracted from the spectrum, such as the ECD peak height of a selected optical transition (S_{11}, S_{22}, S_{33}, or S_{44}) or the ROA intensity of a vibrational mode (e.g., G or 2D). Third, the parameter is normalized using the same procedure as applied during calibration: ECD or ROA peak heights (or areas) are normalized by the corresponding absorption or Raman peak heights (or areas), while maintaining consistency in the treatment of the spectral baseline (i.e., including or excluding it by fitting). Finally, the ee is obtained directly from the corresponding calibration equation, e.g., $ee = a_i \times CD_{norm}$ or $ee = a_i \times ROA_{norm}$ using the fitted coefficients provided in Table 1.

A critical aspect of this methodology is the choice of the normalization procedure. Consistent normalization is essential when comparing datasets between studies or constructing calibration curves. We find that normalization based on peak heights after baseline removal through fitting minimizes systematic deviations arising from residual baselines in the absorption spectra, which may originate from instrumental offsets, scattering contributions, or variations in SWCNT purity.

In conclusion, we present a strategy for absolute ee quantification of enantiomer-sorted (6,5) SWCNT samples by combining HSI, ECD and ROA techniques. Our analysis reveals substantial variability in the (chir)optical responses of SWCNTs across different sample types, which strongly affected ee determination by HSI. These effects were accounted for by using high-quality HiPCO enantiomers (with low number of defects) as reference standards, allowing us to establish universal calibration curves for ECD and ROA. The proposed ee quantification framework is readily applicable to other (*n,m*) chiralities and chiroptical techniques, such as VCD or CPL, enabling improved enantiomer sorting and systematic studies of chirality-dependent phenomena and applications.

Methods

Certain equipment, instruments, software, or materials, commercial or non-commercial, are identified in this paper in order to specify the experimental procedure adequately. Such identification is not intended to imply recommendation or endorsement of any product or service by the National Institute of Standards and Technology (NIST), nor is it intended to imply that the materials or equipment identified are necessarily the best available for the purpose. Unless otherwise noted, uncertainties are reported as one standard deviation.

Preparation of enantiomerically pure (6,5)-SWCNT suspensions

Enantiomerically pure (6,5)-SWCNTs were prepared following methods reported in ref. 18. and explained below. Mixed-chirality SWCNT powders, including CoMoCAT process soots (CHASM, lots#: SG24-0001, SG65i-L58, CG400-P0630)[39] and HiPCO (lot: Rice 189.2)[38] were utilized. These were generally each dispersed at a concentration of 1 mg mL^{-1} in sodium deoxycholate (DOC, Sigma-Aldrich, #30970, >98%) aqueous solution by tip sonication, purified of gross impurities by a centrifugation step, and then subjected to various additional purification steps, as detailed below.

The ATPE process was first used to obtain almost racemic (6,5)-enriched SWCNT samples, referred to as the "parent" samples (S10-Hp and S11-Cp, with H for HiPCO and C for CoMoCAT origin, and p for parent samples). The slight deviation from a perfectly racemic composition in these parent samples (see Supplementary Table 4 for the enantiomeric composition) can be explained by the ATPE protocol itself. This method relies on the preferential interaction of a single-enantiomer chiral surfactant with the two SWCNT enantiomers, which leads to small differences in wrapping efficiency and hydrophilicity and consequently introduces a slight bias toward one of the enantiomers. Through further enantiomeric sorting and extraction of SWCNT fractions at successive steps, we obtained a set of samples with varying enantiomeric purities, as illustrated in Fig. 1c, with dark brown and dark cyan being the most pure (+)-(6,5) and (-)-(6,5) enantiomers, respectively (see Supplementary Note 2.2 on the existing notation of SWCNT enantiomers). Supplementary Table 1 shows a detailed description of the samples, including the filling state, source material, and sorting laboratory.

For the samples prepared at KIT (see Supplementary Table 1), SWCNT powders (CoMoCAT65i CHASM, lot#: SG65i-L58) were dispersed at a concentration of 1 mg mL^{-1} in a 2% (20 g L^{-1}) sodium deoxycholate (DOC, Sigma-Aldrich, #30970, > 98%) aqueous solution by tip sonication (0.9 W mL^{-1}, 45 min, ice bath). After centrifugation (45560× *g*, $g \stackrel{\text{def}}{=} 9.81\ m\ s^{-2}$, Beckman Optima L-80 XP, SW40-Ti rotor, 1 h), 80% of the supernatant was collected as the parent suspension. Then ATPE-based enantiomer separation was carried out according to ref. 18, using a two-phase system of dextran (70 kg mol^{-1}, TCI) and polyethylene glycol (PEG, 6 kg mol^{-1}, Alfa Aesar). ATPE sorting was performed using binary and ternary cosurfactant systems based on DOC, sodium dodecyl sulfate (SDS, Sigma-Aldrich, #436143, > 99%) and sodium cholate (SC, Sigma-Aldrich, #C6445, > 99%). Briefly, the DOC concentration was kept at 0.4 g L^{-1} (0.04%) and SC at 9 g L^{-1} (0.9%), while SDS concentrations were incrementally increased to selectively extract (6,5)-SWCNT enantiomers into the PEG-rich top phase. Specifically, the high-purity (−)-(6,5) enantiomer was isolated

using the binary DOC/SDS system, and the (+)-(6,5) enantiomer using the ternary DOC/SC/SDS system. For this study, only the initial fractions with the highest enantiomer purity were collected from each separation. To remove any remaining metallic species, an additional semiconducting-metallic sorting step was carried out using a surfactant mixture of SC (0.9%), SDS (1%), and DOC (< 0.02%), together with oxidation by sodium hypochlorite (NaClO, 10% to 15% chlorine, Sigma-Aldrich).

For the samples prepared at NIST, enantiomerically separated water-filled CoMoCAT SWCNTs were from a previously dispersed, purified, and length-enriched population generated in the production of NIST RM 8281. In brief, SG65-grade CoMoCAT SWCNT material was dispersed via tip sonication into 20 g L^{-1} sodium deoxycholate (DOC) solution, followed by centrifugation (JA-20 rotor, 1885 rad s^{-1}, 2 h) to remove poorly dispersed material, and subsequently processed by an ultracentrifugation-based length fractionation via an upward race through a dense liquid medium (20 g L^{-1} DOC with 15% mass per volume iodixanol, Beckman Optima L-80 XP, SW-32Ti rotor, 4 °C, 2650 rad s^{-1}, 21 h)[61]. The specific fraction used as the parent for this effort was F11, a fraction containing longer SWCNTs than incorporated into the long fraction of RM 8281[62]. Ultrafiltration using a stirred cell (Millipore) equipped with a 100 kg mol^{-1} membrane was used to remove the iodixanol and adjust the DOC concentration to 10 g L^{-1}. Multistep ATPE was conducted as previously reported[63] to isolate a metallic-species free (6,5)-rich fraction, followed by additional ATPE using essentially the same protocol used at KIT; minor differences were that a DOC concentration of 0.42 g L^{-1} (0.042%) was used, and that both enantiomers were collected from the three-surfactant competition cascade.

Alkane-filled CoMoCAT-type (6,5)-SWCNTs were prepared using CoMoCAT CG400 material (CHASM, lot#: CG400-P0630). Prior to dispersion, these SWCNTs were alkane-filled using a previously reported method[43,44]. Specifically, the SWCNT powder was first oxidized in a 320 °C environment for 30 min using a tube furnace with the tube end open to room air, followed by an annealing step of 1 h at 420 °C in a slowly flowing (few mL s^{-1}) argon gas environment. Filling was accomplished by exposing the oxidized and annealed soot to $C_{24}H_{50}$ (Aldrich T8752, 99%) at 60 °C for seven days. Excess alkane was removed by filtration against a membrane (Millipore VVLP 0.1 µm pore) followed by heptane rinses and refiltration, at which point it was allowed to dry. Dry $C_{24}H_{50}$@CG400 SWCNT powder was dispersed at a concentration of 1 mg mL^{-1} in a 20 g L^{-1} DOC aqueous solution by tip sonication (0.9 W mL^{-1}, 35 min, ice bath). Initial centrifugation (SW-32Ti rotor, 20 °C, 2200 rad s^{-1}, 1 h, collecting the supernatant by decanting) was followed by rate-zonal ultracentrifugation over a 9.5% mass per volume iodixanol, 10 g L^{-1} DOC race layer (VTi50 rotor, 5236 rad s^{-1}, 2 h 45 min) collecting the main band in the center of the centrifuge tube[63]. Ultrafiltration using a stirred cell (Millipore) equipped with a 100 kg mol^{-1} membrane was used to remove the iodixanol and adjust the DOC concentration to 10 g L^{-1}. Multistep ATPE was conducted as previously reported[63] to isolate a metallic-species free (6,5)-rich fraction. This dispersion was then fractionated by length to remove the short, <≈ 200 nm long, SWCNTs using polymer depletion-based length separation (PDLS) with 3.6% mass per mass poly methacrylic acid sodium salt (PMAA) as reported in ref. 64., collecting the pellet fraction. The redispersed pellet (long (6,5)-rich SWCNT) was then fractionated using the same ATPE enantiomer separation process as above.

HiPCO SWCNTs (Rice HiPCO: lot 189.2) were prepared at NIST by dispersing at a concentration of 1 mg mL^{-1} in a 20 g L^{-1} DOC aqueous solution by tip sonication (≈ 0.9 W mL^{-1}, 30 min, ice bath). Initial centrifugation (SW-32Ti rotor, 20 °C, 2324 rad s^{-1}, 1 h, collecting the supernatant by decanting) was followed by PDLS length separation at 4.0% mass per mass PMAA, collecting the pellet and redispersing it in 10 g L^{-1} DOC. Rate-zonal ultracentrifugation was then performed over a 10% mass per volume iodixanol, 10 g L^{-1} DOC, race layer (VTi65.2 rotor, 6806 rad s^{-1}, 1 h) collecting the main band in the center of the centrifuge tube[63]. Ultrafiltration using a stirred cell (Millipore) equipped with a 100 kg mol^{-1} membrane was used to remove the iodixanol and adjust the DOC concentration to 10 g L^{-1}. Multistep ATPE was conducted as above to isolate a metallic-species free (6,5)-rich fraction, followed by ATPE for enantiomer separation also as described above.

Finally, all purified (6,5)-SWCNT fractions were concentrated and adjusted to 10 g L^{-1} DOC by iterative ultrafiltration using a stirred cell (Millipore) equipped with a 100 or 300 kg mol^{-1} membrane. Sample names were given in order of purity, with S01 being the purest (+) enantiomer and S17 the purest (-) chirality, C stands for CoMoCAT and H for HiPCO origin.

Hyperspectral fluorescence microscopy

SWCNT samples were first prepared for the HSI measurements. In particular, to preserve the specific differences in stacking of the DOC surfactant molecules on the SWCNT walls of both enantiomers, the SWCNTs are embedded in a thin slab of a transparent tetramethyl orthosilicate (TMOS) gel matrix sandwiched between two microscope slides which was previously demonstrated to not affect the emission properties (intensity, wavelength, line width) of the SWCNTs[35]. Moreover, by making the slab sufficiently thin, and after proper surface treatment of the microscope slides, the SWCNTs do not interact with the glass surface and remain primarily in one focal plane so that their entire length is in focus. Prior to pipetting, the plasma cleaned (10 min, 18 W at an ambient air flow of 23 mL min-1, PDC-32G-2, Harrick Plasma (S.A.F.I.R.)) glassware were given a hydrophobic coating (Rain-X) to minimize the possible interactions with the hydrophilic surfactant-coated SWCNTs.

SWCNTs were excited using a 568 nm continuous-wave optically pumped semiconductor laser (Sapphire 568 LP, Coherent) in a wide-field configuration, producing an excitation intensity of ≈12 W cm^{-2}. Although the polarization direction of the linearly polarized light of the laser compared to the SWCNT orientation in the sample influences the excitation efficiency, since the SWCNTs are all oriented randomly, this effect is compensated for by acquiring a sufficiently large sample size. The generated SWCNT PL was imaged using an inverted, infinity-corrected epifluorescence microscope (Eclipse Ti-U, Nikon) equipped with a brightfield, 60 × oil-immersion objective (CFI Plan Apo Lambda 60x Oil, Nikon), a 775 nm long-pass filter cube, and a liquid-nitrogen-cooled 2D Si CCD camera (PyLoN:400BR_eXcelon, Princeton Instruments). Hyperspectral images were acquired from 935–1035 nm in 5 nm steps using a liquid crystal tunable filter (VariSpec LNIR, 850–1800 nm) with 5 accumulations for each emission wavelength and an exposure time of 1.5 and 2 s for the HiPCO and CoMoCAT samples respectively.

The wavelength-dependent PL background, including the detector's dark current, was measured analogously at a position in the microscope sample where no SWCNTs were present (same focal plane as the imaged SWCNTs). The hyperspectral images were corrected for the wavelength-dependent background PL and the spatial (flatfield) and spectral sensitivity of the setup, as explained in detail in ref. 35.

The HSI histograms were generated employing a previously-developed convolutional neural network that identifies those pixels of in-focus SWCNTs, while out-of-focus SWCNTs and background pixels could be discarded, similarly as in ref. 35. Before spectroscopic analysis of the PL spectra for each individual in-focus SWCNT, a morphological improvement was performed (see Supplementary Note 3.1) and contiguous sets of SWCNT pixels were grouped together when originating from an individual SWCNT, summing the PL intensities from these pixels, such that a single PL spectrum is obtained for each SWCNT in the image. Aside from that, the length of each SWCNT was determined, by calculating its skeleton similarly as was performed in ref. 35, so that calibration of the HSI histograms was possible. The total number of

individual nanotubes included in the bivariate histograms (Figs. 2b and 3a–c) is reported in Supplementary Note 4.1.

Each individual PL spectrum was then fitted, similarly as in ref. 35. and explained in detail in Supplementary Note 3.1, and for each SWCNT the length, total intensity, line width in FWHM, and the S_{11} peak position was retained to create the HSI histograms. Data from ill-conditioned fits were removed, e.g., from too noisy PL spectra or from other SWCNT chiralities prior to analyzing the HSI histograms.

Fitting of the HSI histograms

To extract the relative contributions of empty and water-filled (+)–(6,5) and (−)–(6,5) SWCNTs, we analyzed the experimental bivariate HSI histograms using simultaneous fitting of correlated two-dimensional distributions. To reliably resolve small fractions of one enantiomer in samples dominated by the opposite enantiomer, histograms from samples derived from the same parent SWCNT solution but with different enantiomer ratios were fitted jointly. In this procedure, all line-shape parameters were constrained to be identical across datasets, while only the relative amplitudes were allowed to vary, and all parameters were optimized by least-squares minimization.

Compared to earlier work on racemic (6,5) HiPCO SWCNTs[35], the present data exhibit additional spectral features, overlapping tails between low- and high-energy regions, and pronounced deviations from purely Gaussian statistics. These characteristics indicate the presence of multiple underlying distributions beyond the four contributions previously required. The final model therefore combines two sharp normal bivariate Gaussian components for empty (+) and (-)-(6,5) SWCNTs, a sum of two normal Gaussian distributions for each water-filled enantiomer (one sharp and one broader underlying component to mimic the tail of the distribution) and two skewed Gaussian distributions to fit defective SWCNTs in zone L. The combination of these peaks yields an excellent overall agreement with the experiment. The analysis of the residuals confirms the quality of the fits, with only about 4%–5% of the total counts not captured by the model, providing an upper bound as it includes inherent statistical noise in the data. The exact fit model is described in full detail in Supplementary Note 4.3.

ECD and absorbance spectroscopy

ECD and absorbance spectra were recorded using a Chirascan-plus spectrometer (Applied Photophysics) equipped with a Peltier temperature-controlled cell holder. Measurements were performed at room temperature ($T = 21\,°C$) over a wavelength range of 200 to 1050 nm, with a step size of 1 nm, a bandwidth of 1 nm, and an accumulation time of 1 s per point. A path length of 3 mm was used for all measurements. The sample spectra were corrected by subtracting the solvent spectrum (H_2O or D_2O), which was recorded under identical conditions. To verify the reproducibility of the CD and absorption measurements (Supplementary Note 6.1), we recorded CD spectra of the HiPCO samples also using a JASCO J-1500 spectrometer over the range 800 nm to 200 nm, with a 1 mm path length cuvette, 0.1 nm step size, 100 nm min^{-1} scanning speed, and ≈2.2 nm bandwidth.

To determine the intensities, we fitted the ECD and absorption spectra using a set of Lorentzian functions. The fitting parameters were optimized independently for each spectrum (examples of the data fitting procedure are given in the Supplementary Note 6.2).

Photoluminescence excitation-emission (PLE) spectroscopy

To assess the purity of the HiPCO samples in terms of their (n,m) species distribution (i.e., not enantiomeric purity), wavelength-dependent infrared PLE maps were recorded (Supplementary Fig. 2), using a dedicated in-house developed setup. The sample is excited with a pulsed Xe-lamp (Edinburgh Instruments, custom adapted Xe900/XP920) using a 300 mm focal length monochromator (Acton SpectraPro 2355). The excitation wavelength is varied in 5 nm steps from 400 to 1200 nm using a 1200 g mm^{-1} grating with a slit-selected average resolution of 6 nm. The fluorescence is detected under a 90° angle using a 150 mm focal length spectrograph (Acton SpectraPro 2156) with a 150 g mm^{-1} grating with a slit-selected average resolution of 6 nm, and with a liquid nitrogen cooled InGaAs photodiode array detector with a sensitivity up to 1.65 µm (Princeton Instruments Pylon IR: 1024-1.7). All PLE maps were corrected for detector and spectrograph efficiency, filter transmission, and spectral and temporal variations of the excitation intensity. Moreover, PLE maps were also corrected for (re)absorption of the excitation and emitted light, using the absorption spectrum of the samples measured just before the PLE experiment. These absorption spectra were measured from 200 nm to 2500 nm using a Cary 5000 UV-vis-NIR spectrometer (Supplementary Fig. 3). A 60 µL quartz microcell with a 3 mm path length was used to contain the samples. All absorption spectra were baseline corrected with a 1% mass per volume DOC/D_2O or DOC/H_2O solution, depending on the sample. Any additional contributions in the D_2O samples due to trace amounts of H_2O (that naturally arise over time) were subtracted afterward. Due to the saturated absorption bands of H_2O and D_2O in the 3 mm path length cells, this baseline results in a high noise level around 1700 nm or 2000 nm, respectively.

Raman optical activity

The experimental ROA spectra were measured using a custom-built instrument based on the Hug and Hangartner design[65] (Supplementary Fig. 1). A 532 nm diode-pumped solid-state laser (Laser Quantum Gem 532) served as the excitation source. The beam first passed through a Glan–Taylor polarizer (Leysop) to enhance linear polarization, then through two continuously rotating half-wave plates (181 Hz, Koford Engineering, series 4851) to depolarize it, and was finally focused into the sample solution using a plano-convex lens ($f = 50$ mm, f/2.0, Thorlabs).

The same lens collected the back-scattered light, which was collimated and directed through a 532 nm long-pass edge filter (Semrock RazorEdge 532 nm) to remove Rayleigh scattering. The filtered beam entered a circular polarization analyzer composed of a liquid-crystal retarder (LVR-300-VIS-1L-TSC, Meadowlark Optics) and two polarizing beam-splitter cubes (Thorlabs), separating the left- and right-circularly polarized components into two distinct beams.

These beams were focused by achromatic doublets ($f = 60$ mm, f/2.4) onto the two inputs of a Y-shaped round-to-linear fiber bundle (2 × 18 fibers, 75 µm core, Ceramoptec). The linear output of the bundle was coupled to an Andor Kymera 328i spectrograph equipped with three transmission gratings, and the dispersed light was detected by a CCD camera (Andor Newton DU920P-BVF).

A four-phase virtual enantiomer deterministic offset correction scheme[66] was implemented using half-wave plates mounted on motorized translation stages (Thorlabs) in both the incident and collected light paths (circularity converters CC1 and CC2 in Supplementary Fig. 1). In addition, a continuously rotating half-wave plate was placed in the collected beam (11 Hz rotation, Faulhaber, series 1628-B) to temporally average residual linear polarization components[66].

Acquisition time and laser power were optimized for each measurement to maximize the signal-to-noise ratio by increasing CCD counts while avoiding sample heating, which was monitored via shifts of the G-band. These acquisition parameters depend strongly on the SWCNT concentration. For a typical (6,5) SWCNT sample, the concentration was intentionally kept low to avoid ECD–Raman effects (S_{22} peak height at ≈570 nm <0.67 cm^{-1}). Under these conditions, an ROA spectrum (Fig. 2c) was acquired in ≈60 min using ≈90 mW of laser power at the sample. Concentration-dependent (Fig. 6e) and focus-dependent measurements (Supplementary Fig. 25) were performed at 40 mW with acquisition times of ≈10 and ≈2 min, respectively. The solvent (H_2O) spectrum was not subtracted from the SWCNT spectra, as it is featureless in the spectral region of interest, while any residual

background was accounted for during spectral fitting using a linear baseline. The ROA and Raman spectra were fitted by a set of Voigt functions, which were implemented through the Faddeeva function of complex arguments, using the C++ package by Steven G. Johnson at MIT[67]. The fitting parameters were optimized independently for each spectrum (examples of the data fitting procedure are given in the Supplementary Note 7.2).

Resonant Raman spectroscopy

Resonant Raman measurements were performed in backscattering geometry using a Dilor XY800 triple spectrometer operated in high dispersion mode and equipped with a liquid-nitrogen-cooled CCD detector. A 561 nm (Cobolt Jive) laser was used for excitation. The recorded spectra were corrected for the instrumental spectral sensitivity and the wavelength calibration of the spectrometer. Afterwards the data was fitted using a sum of 2 or 3 Lorentzian contributions corresponding to empty, water-filled, alkane-filled or defective SWCNTs.

Reporting summary

Further information on research design is available in the Nature Portfolio Reporting Summary linked to this article.

Data availability

The data that support the findings of this study, including HSI, ECD, and ROA data, are available from Figshare[68] and from the corresponding authors upon request. Unprocessed raw data are provided as Supplementary Data 1. Source data are provided with this paper.

Code availability

The code that was used to process the raw data is available from the corresponding authors upon request.

References

1. Kotov, N. A., Liz-Marzán, L. M. & Weiss, P. S. Chiral nanostructures: new twists. *ACS Nano* **15**, 12457–12460 (2021).
2. Aiello, C. D. et al. A chirality-based quantum leap. *ACS Nano* **16**, 4989–5035 (2022).
3. Naaman, R., Paltiel, Y. & Waldeck, D. H. Chiral molecules and the electron spin. *Nat. Rev. Chem.* **3**, 250–260 (2019).
4. Crassous, J. et al. Materials for chiral light control. *Nat. Rev. Mater.* **8**, 365–371 (2023).
5. Genet, C. Chiral light-chiral matter interactions: an optical force perspective. *ACS Photonics* **9**, 319–332 (2022).
6. Juraschek, D. M. et al. Chiral phonons. *Nat. Phys.* 21, 1532–1540. (2025).
7. Pu, C., Xu, Y., Liu, Q., Zhu, A. & Shi, G. Enantiomers of single chirality nanotube as chiral recognition interface for enhanced electrochemical chiral analysis. *Anal. Chem.* **91**, 3015–3020 (2019).
8. Wu, Q., Lv, H. & Zhao, L. Applications of carbon nanomaterials in chiral separation. *TrAC - Trends Analyt. Chem.* **129**, 115941 (2020).
9. Jiang, S. & Kotov, N. A. Circular Polarized Light Emission in Chiral Inorganic Nanomaterials. *Advanced Materials* **35**, 1–19 (2023).
10. Firouzeh, S., Hossain, M. A., Cuerva, J. M., Álvarez de Cienfuegos, L. & Pramanik, S. Chirality-induced spin selectivity in composite materials: a device perspective. *Acc. Chem. Res.* **57**, 1478–1487 (2024).
11. Rahman, M. W. et al. Chirality-induced spin selectivity in hetero-chiral short-peptide-carbon-nanotube hybrid networks: role of supramolecular chirality. *ACS Nano* **16**, 16941–16953 (2022).
12. Hao, J. et al. Direct detection of circularly polarized light using chiral copper chloride–carbon nanotube heterostructures. *ACS Nano* **15**, 7608–7617 (2021).
13. Reich, S., Thomsen, C. & Maultzsch, J. *Carbon Nanotubes: Basic Concepts and Physical Properties* (WILEY-VCH Verlag GmbH & Co. KGaA, 2004).
14. Rao, R. et al. Carbon nanotubes and related nanomaterials: critical advances and challenges for synthesis toward mainstream commercial applications. *ACS Nano* **12**, 11756–11784 (2018).
15. Wei, X. et al. Recent advances in structure separation of single-wall carbon nanotubes and their application in optics, electronics, and optoelectronics. *Adv. Sci.* **9**, 1–42 (2022).
16. Yang, F. et al. Chirality pure carbon nanotubes: growth, sorting, and characterization. *Chem. Rev.* **120**, 2693–2758 (2020).
17. Li, H. et al. Separation of specific single-enantiomer single-wall carbon nanotubes in the large-diameter regime. *ACS Nano* **14**, 948–963 (2020).
18. Li, H. et al. Isolation of the (6,5) single-wall carbon nanotube enantiomers by surfactant-assisted aqueous two-phase extraction. *Carbon* **204**, 475–483 (2023).
19. Leung, D., Kang, S. O. & Anslyn, E. V. Rapid determination of enantiomeric excess: a focus on optical approaches. *Chem. Soc. Rev.* **41**, 448–479 (2012).
20. Abd El-Mageed, A. I. A. & Ogawa, T. Single-walled carbon nanotube absolute-handedness chirality assignment confirmation using metalized porphyrin's supramolecular structures via STM imaging technique. *Chirality* **32**, 345–352 (2020).
21. Meyer, R. R. et al. A composite method for the determination of the chirality of single walled carbon nanotubes. *J. Microsc.* **212**, 152–157 (2003).
22. Liu, Z. et al. Determination of optical isomers for left-handed or right-handed chiral double-wall carbon nanotubes. *Phys. Rev. Lett.* **95**, 187406 (2005).
23. Bernaerts, D., De Beeck, M. O., Amelinckx, S., van Landuyt, J. V. & van Tendeloo, G. V. The chirality of carbon nanotubules determined by dark-field electron microscopy. *Philosoph. Mag. A* **74**, 723–740 (1996).
24. Chen, Y. et al. Chiral structure determination of aligned single-walled carbon nanotubes on graphite surface. *Nano Lett* **13**, 5666–5671 (2013).
25. Chen, Y. et al. Helicity-dependent single-walled carbon nanotube alignment on graphite for helical angle and handedness recognition. *Nat. Commun.* **4**, 2205 (2013).
26. Wei, X. et al. Experimental determination of excitonic band structures of single-walled carbon nanotubes using circular dichroism spectra. *Nat. Commun.* **7**, 12899 (2016).
27. Sato, N., Tatsumi, Y. & Saito, R. Circular dichroism of single-wall carbon nanotubes. *Phys. Rev. B* **95**, 155436 (2017).
28. Sebastian, F. L. et al. Circular dichroism of quantum defects in carbon nanotubes created by photocatalytic oxygen functionalization. *Nat. Commun.* **16**, 5107 (2025).
29. Magg, M., Kadria-Vili, Y., Oulevey, P., Weisman, R. B. & Bürgi, T. Resonance Raman optical activity spectra of single-walled carbon nanotube enantiomers. *J. Phys. Chem. Lett.* **7**, 221–225 (2016).
30. Nagy, P. R., Koltai, J., Surján, P. R., Kürti, J. & Szabados, Á Resonance Raman optical activity of single walled chiral carbon nanotubes. *J. Phys. Chem. A.* **120**, 5527–5538 (2016).
31. Lu, F. et al. Achiral Plasmon nanostructures for identifying single-walled carbon nanotube enantiomers via enhancing their Raman optical activity. *ACS Appl. Nano Mater* **8**, 2000–2005 (2025).
32. Yao, F. et al. Complete structural characterization of single carbon nanotubes by Rayleigh scattering circular dichroism. *Nat. Nanotechnol.* **16**, 1073–1078 (2021).
33. Wei, X., Tanaka, T., Hirakawa, T., Yomogida, Y. & Kataura, H. DeterminAtion Of Enantiomeric Purity Of Single-wall Carbon Nanotubes Using Flavin Mononucleotide. *J. Am. Chem. Soc.* **139**, 16068–16071 (2017).

34. Sim, J. et al. Determination of the absolute enantiomeric excess of the carbon nanotube ensemble by symmetry breaking using the optical titration method. *Langmuir* **33**, 11000–11009 (2017).
35. Erkens, M. et al. Hyperspectral detection of the fluorescence shift between chirality-sorted empty and water-filled single-wall carbon nanotube enantiomers. *ACS Nano* **18**, 14532–14545 (2024).
36. He, Y., Wang, B., Dukor, R. K. & Nafie, L. A. Determination of absolute configuration of chiral molecules using vibrational optical activity: a review. *Appl. Spectrosc.* **65**, 699–723 (2011).
37. Tsukamoto, M. & Kagan, H. B. Recent advances in the measurement of enantiomeric excesses. *Adv. Synth. Catal.* **344**, 453–463 (2002).
38. Duque, J. G. et al. Diameter-dependent solubility of single-walled carbon nanotubes. *ACS Nano* **4**, 3063–3072 (2010).
39. Bachilo, S. M. et al. Narrow (n,m)-distribution of single-walled carbon nanotubes grown using a solid supported catalyst. *J. Am. Chem. Soc.* **125**, 11186–11187 (2003).
40. Cambré, S. & Wenseleers, W. Separation and diameter-sorting of empty (end-capped) and water-filled (open) carbon nanotubes by density gradient ultracentrifugation. *Angew. Chem. Int. Ed.* **50**, 2764–2768 (2011).
41. Cambré, S. et al. Luminescence properties of individual empty and water-filled single-walled carbon nanotubes. *ACS Nano* **6**, 2649–2655 (2012).
42. Wenseleers, W., Cambré, S., Čulin, J., Bouwen, A. & Goovaerts, E. Effect of water filling on the electronic and vibrational resonances of carbon nanotubes: characterizing tube opening by Raman spectroscopy. *Adv. Mater.* **19**, 2274–2278 (2007).
43. Qu, H. et al. Selective filling of n-hexane in a tight nanopore. *Nat. Commun.* **12**, 1–8 (2021).
44. Streit, J. et al. Alkane encapsulation induces strain in small-diameter single-wall carbon nanotubes. *J. Phys. Chem. C.* **122**, 11577–11585 (2018).
45. Campo, J. et al. Optical property tuning of single-wall carbon nanotubes by endohedral encapsulation of a wide variety of dielectric molecules. *ACS Nano* **15**, 2301–2317 (2021).
46. Campo, J. et al. Enhancing single-wall carbon nanotube properties through controlled endohedral filling. *Nanoscale Horiz* **1**, 317–324 (2016).
47. Machalska, E. et al. Recognition of the True and False Resonance Raman Optical Activity. *Angewandte Chemie* **133**, 21375–21380 (2021).
48. Li, G. et al. Can one measure resonance Raman optical activity? *Angew. Chem. Int. Ed.* **60**, 22004–22009 (2021).
49. Vierck, A., Gannott, F., Schweiger, M., Zaumseil, J. & Maultzsch, J. ZA-derived phonons in the Raman spectra of single-walled carbon nanotubes. *Carbon.* **117**, 360–366 (2017).
50. Tyborski, C., Vierck, A., Narula, R., Popov, V. N. & Maultzsch, J. Double-resonant Raman scattering with optical and acoustic phonons in carbon nanotubes. *Phys. Rev. B* **97**, 214306 (2018).
51. Nafie, L. A. Theory of resonance Raman optical activity: The single electronic state limit. *Chem. Phys.* **205**, 309–322 (1996).
52. Wei, X. et al. Length-dependent enantioselectivity of carbon nanotubes by gel chromatography. *ACS Nano* **17**, 8393–8402 (2023).
53. Liang, K. et al. Negative nonlinear CD-ee dependence in polycrystalline BINOL thin films. *J. Am. Chem. Soc.* **145**, 27933–27938 (2023).
54. Panagiotopoulou, C. et al. Chiroptical amplification beyond enantiopurity in chiral films. *Adv. Opt. Mater.* **13**, 1–6 (2025).
55. Yao, L. et al. Amplification of chirality in self-assembled chiral perovskite superstructure films. *J. Am. Chem. Soc.* **147**, 36420–36427 (2025).
56. Wu, T. et al. Two spectroscopies in one: interference of circular Dichroism and Raman optical activity. *Angew. Chem. Int. Ed.* **59**, 21895–21898 (2020).
57. Sanchez, S. R., Bachilo, S. M., Kadria-Vili, Y., Lin, C. W. & Weisman, R. B. n,m)-Specific Absorption Cross Sections of Single-Walled Carbon Nanotubes Measured by Variance Spectroscopy. *Nano Lett.* **16**, 6903–6909 (2016).
58. Schöppler, F. et al. Molar extinction coefficient of single-wall carbon nanotubes. *J. Phys. Chem. C.* **115**, 14682–14686 (2011).
59. Streit, J. K., Bachilo, S. M., Ghosh, S., Lin, C.-W. & Weisman, R. B. Directly measured optical absorption cross sections for structure-selected single-walled carbon nanotubes. *Nano Lett* **14**, 1530–1536 (2014).
60. Oudjedi, L., Parra-Vasquez, A. N. G., Godin, A. G., Cognet, L. & Lounis, B. Metrological investigation of the (6,5) carbon nanotube absorption cross section. *J. Phys. Chem. Lett.* **4**, 1460–1464 (2013).
61. Fagan, J. A. et al. Centrifugal length separation of carbon nanotubes. *Langmuir* **24**, 13880–13889 (2008).
62. NIST, Standard reference materials. https://www.nist.gov/srm.
63. Fagan, J. A. Aqueous two-polymer phase extraction of single-wall carbon nanotubes using surfactants. Nanoscale Adv. **1**, 3307–3324 (2019).
64. Shapturenka, P., Barnes, B. K., Mansfield, E., Noor, M. M. & Fagan, J. A. Universalized and robust length separation of carbon and boron nitride nanotubes with improved polymer depletion-based fractionation. *RSC Adv.* **14**, 25490–25506 (2024).
65. Hug, W. & Hangartner, G. A novel high-throughput Raman spectrometer for polarization difference measurements. *J. Raman. Spectrosc.* **30**, 841–852 (1999).
66. Hug, W. Virtual enantiomers as the solution of optical activity's deterministic offset problem. *Appl. Spectrosc.* **57**, 1–13 (2003).
67. Faddeeva-Voigt function, S. G. Johnson, Faddeeva package. http://ab-initio.mit.edu/faddeeva/ (2012).
68. López Carrillo, M. Á. et al. Absolute quantification of enantiomeric purity of sorted carbon nanotubes by correlating hyperspectral fluorescence microscopy with ensemble chir-optical spectroscopy. Figshare https://doi.org/10.6084/m9.figshare.31891381 (2026).

Acknowledgements

We thank X. Wei for providing absorption and ECD spectra of enantiomer-sorted CoMoCAT and HiPCO (6,5) SWCNTs from refs. 33,52, which we used to test our fitting scripts and verify the specific ECD normalization.

Author contributions

D.L., S.C. and W.H. conceived the study and designed the experiments. J.E.F., M.Z., H.L. and B.S.F. prepared the enantiomer-sorted SWCNT samples. Under the supervision of S.C. and W.W., M.E. constructed the HSI setup and M.A.L.C. performed HSI measurements and data processing. F.D. developed the original ROA setup, which D.L. adapted for SWCNT measurements. D.L. performed all ECD and ROA experiments and analyzed the data. D.L. and S.C. developed the model used to fit the bivariate HSI histograms. S.C. conducted UV-Vis-NIR, PLE, and high-resolution Raman measurements on selected samples. D.L. and S.C. wrote the manuscript with input from all coauthors. All authors participated in data interpretation and discussion.

Funding

This work was financially supported by the Research Foundation of Flanders (FWO) through projects with grant numbers G036618N (S.C., W.W.), G021112N (W.W.), and G0AAM25N (S.C., W.H.) and a personal PhD grant for M.E. M.A.L.C. acknowledges support from the Research Fund from the University of Antwerp through a BOF-DOCPRO4 project. S.C. and W.H. acknowledge support from the CASCH center of excellence. H.L. acknowledges support from the Turku Collegium for Science, Medicine and Technology (TCSMT). J.A.F and M.Z. were entirely

supported by internal National Institute of Standards and Technology funding.

Competing interests
The authors declare no competing interests.

Additional information
Supplementary information The online version contains supplementary material available at https://doi.org/10.1038/s41467-026-73397-2.

Correspondence and requests for materials should be addressed to Sofie Cambré or Dmitry I. Levshov.

[1]Theory and Spectroscopy of Molecules and Materials, Department of Chemistry and Department of Physics, University of Antwerp, Antwerp, Belgium. [2]Nanostructured and Organic Optical and Electronic Materials, Department of Physics, University of Antwerp, Antwerp, Belgium. [3]Royal Belgian Institute for Space Aeronomy, Brussels, Belgium. [4]Materials Science and Engineering Division, National Institute of Standards and Technology, Gaithersburg, MD, USA. [5]Institute of Nanotechnology, Karlsruhe Institute of Technology, Karlsruhe, Germany. [6]Department of Mechanical and Materials Engineering, University of Turku, Turku, Finland. [7]Turku Collegium for Science, Medicine and Technology, University of Turku, Turku, Finland. ✉e-mail: sofie.cambre@uantwerpen.be; dmitry.levshov@uantwerpen.be